remote sensing

MDPI

Technical Note

Evaluation of Satellite Images and Products for the Estimation of Regional Reference Crop Evapotranspiration in a Valley of the Ecuadorian Andes

Fernando Oñate-Valdivieso *, Arianna Oñate-Paladines and Deiber Núñez

Department of Civil Engineering, Hydrology and Climatology Research Group, Universidad Técnica Particular de Loja, C/. Marcelino Champagnat S/N, Loja 1101608, Ecuador
* Correspondence: fronate@utpl.edu.ec

Abstract: The capabilities of images and products obtained by four satellite sensors with different spatial and temporal resolutions (LANDSAT 8, ASTER, MODIS and SENTINEL 3) were analyzed as inputs for the calculation of the reference crop evapotranspiration (ETo). The FAO Penman-Monteith equation was: (a) used in a traditional way, to calculate local values of ETo using data recorded in the existing meteorological stations in the study area; and (b) applied to estimate the regional ETo using the images and products obtained through remote sensing. The capabilities of the satellite products selected were evaluated by means of cross-validation, comparing the values obtained by the meteorological stations to the corresponding values extracted from the regional evapotranspiration maps. The coefficient of determination (R^2), the Nash–Sutcliffe efficiency (NSE) and the root mean square error (RMSE) were calculated. The results of the study show that there is a direct correlation between the spatial resolution and the accuracy of the ETo estimates, the products of LANDSAT 8 being those that reached the greatest accuracy. Nevertheless, for continuous ETo monitoring, SENTINEL 3 is preferred.

Keywords: evapotranspiration; Penman-Monteith equation; remote sensing

check for updates

Citation: Oñate-Valdivieso, F.; Oñate-Paladines, A.; Núñez, D. Evaluation of Satellite Images and Products for the Estimation of Regional Reference Crop Evapotranspiration in a Valley of the Ecuadorian Andes. *Remote Sens.* **2022**, *14*, 4630. https://doi.org/10.3390/rs14184630

Academic Editor: Pradeep Wagle

Received: 20 July 2022
Accepted: 9 September 2022
Published: 16 September 2022

1. Introduction

The spatial and temporal variation of evapotranspiration has great importance for hydrological, environmental, forestry and agricultural applications. Evapotranspiration (ET) represents the loss of water from a surface through the simultaneous processes of evaporation and transpiration [1]. ET is generally measured using ground-based instruments, such as lysimeters, tank evaporators, or eddy covariance systems. However, ground measurements have limited ability to provide representative values because measurement network densities tend to be low [2], reducing their practical applicability. In contrast, the application of indirect methods based on empirical and semi-empirical equations that use meteorological data present greater relevance. Widely accepted methodologies include those proposed by Thornwaite and Mather; Turc, Blanney and Criddle; and Penman and Monteith [3].

Reference crop evapotranspiration (ETo) is defined as the rate of evapotranspiration from a hypothetical reference crop with an assumed crop height of 0.12 m, a fixed daily canopy resistance of 70 s m−1 and an albedo of 0.23, closely resembling the evaporation from an extensive surface of green grass cover of uniform height, actively growing and adequately watered [4].

ETo depends on the characteristics of the soil and vegetation, so it can present notable spatial variation. However, the direct and indirect methods have limitations in representing this variation because they are not spatially distributed.

ETo is usually calculated by applying the FAO Penman-Monteith equation, which requires information on temperature, solar radiation, wind speed and relative humidity.

These variables are usually recorded through meteorological station networks. However, in the Andes, these networks lack sufficient density and the necessary instruments to record all required parameters. To compensate for this, remote sensing strategies for monitoring and studying ETo at different spatial and temporal scales have been used for several decades [5–11], showing that it is possible to determine ETo in large areas by applying techniques based on remote sensing even where climate data are not available.

Methodologies for calculating ET using remote sensing data can be grouped into the following categories: (a) surface energy balance methods [12–15], (b) surface temperature and vegetation index methods [16–19], (c) methods based on the Penman–Monteith equation [20–22], (d) methods based on the Priestley–Taylor equation [23,24], (e) empirical methods [25] and (f) water balance-based methods [26,27].

Currently there are different kinds of satellite data, with various spatial, temporal and radiometric resolutions, applicable for the calculation of ETo. Satellite images are an excellent source for constant and frequent observation of the Earth's surface in near real time [28]. In this work, the images and products obtained by remote sensing were analyzed to evaluate their potential for calculation of the reference crop evapotranspiration in an Andean zone in Ecuador.

2. Materials and Methods

2.1. Study Area

The study area is located in the province of Loja (Ecuador) between the coordinate points 79°13′29.8″W, 03°55′35.9″S and 79°12′08.8″W, 04°08′16.4″S. The city of Loja (240,000 inhabitants) is located in the valley, surrounded by large areas of forest and grassland. The valley is limited by the eastern and western branches of the Andes mountain range. The study area has an altitude range of 2102 to 3400 m [29]. Its climate is sub-humid equatorial temperate, with an average temperature of 16.6 °C and an average annual rainfall of 909 mm, presenting a dry season between May and November and a rainy season between December and April [30]. The location of the study area is presented in Figure 1.

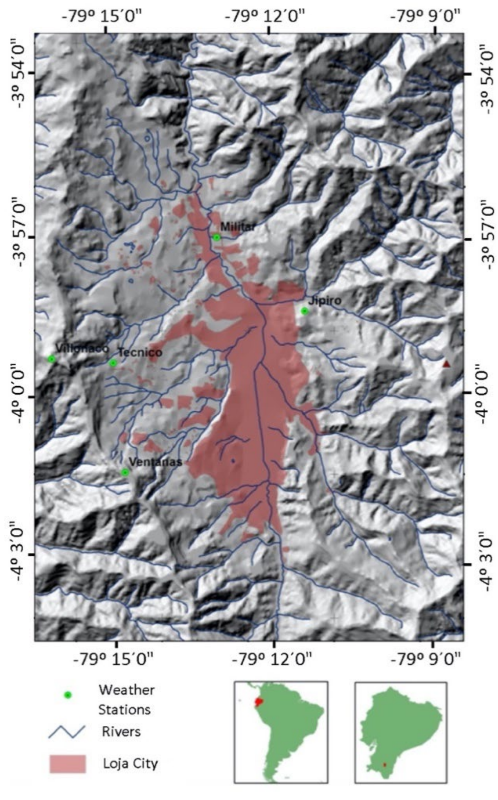

Figure 1. Location of study area.

2.2. The Penman–Monteith Equation

The FAO Penman-Monteith equation [4] is the most widely used equation for the estimation of the reference crop evapotranspiration. The FAO Penman-Monteith equation may be expressed as:

$$ET_O = \frac{0.408\Delta(R_n - G) + \gamma\frac{900}{T+273}U_2(e_s - e_a)}{\Delta + \gamma(1 + 0.34U_2)} \quad (1)$$

where ETo is the reference evapotranspiration (mm d^{-1}), T is the daily air temperature at 2 m height (°C), Δ is the slope of the vapor pressure curve (kPa °C^{-1}), γ is the psychrometric constant (kPa °C^{-1}), $(e_s - e_a)$ is the saturation vapor pressure deficit (kPa), R_n is the net radiation flux on the crop surface (Mj m^2 day $^{-1}$), G is the sensible heat flux into the soil (Mj m^2 d^{-1}) and U_2 is the wind speed at 2 m above ground (m s^{-1}).

The FAO Penman-Monteith equation is used in this work with two different approaches: (a) to calculate the ETo in a traditional way, using data recorded in the meteorological stations available in the study area and (b) to estimate the regional ETo using images and products obtained by remote sensing. The values calculated at the meteorological stations were used to validate the results obtained using satellite data.

2.3. Information Collected

Three image sets from the LANDSAT 8 Operational Land Imager (OLI) Thermal Infrared Sensor (TIRS), two image sets from the Advanced Spaceborne Thermal Emission and Reflection Radiometer (ASTER) and six product sets from the Moderate Resolution Imaging Spectroradiometer (MODIS) and Land Surface Temperature and Emissivity (MOD11)—Vegetation Indices (MOD13) were collected for the study area from the USGS EarthExplorer server [31]. Additionally, four image sets from the SENTINEL 3 Ocean and Land Color Instrument (OLCI) Sea and Land Surface Temperature Radiometer (SLSTR) were obtained from the ESA Copernicus portal [32]. Their acquisition dates, spectral bands and spatial resolutions are listed in Table 1.

Table 1. Satellite products considered.

Resolution	Satellite Data			
	LANDSAT 8	**SENTINEL 3**	**ASTER**	**MODIS.**
Radiometric (bits)	16	-	8–16	12
Spatial (m)	30 (Coastal/Aerosol) 30 (B,G,R,NIR,SWIR) 100 (TIR)	500 (S1-S60) 1000 (S7-S9)	15 (VNIR) 30 (SWIR) 90 (TIR)	250 (B1-2) 500(B3-7) 1000 (B8-36)
Spectral (bands)	11	11 (SLSTR) 21 (OLCI)	14	36
Temporal (days)	16	2 (SLSTR) 1 (OLCI)	16	1
Acquisition dates	7 January 2017 19 August 2017 20 September 2017	7 May 2017 24 June 2017 14 July 2017 20 September 2017	7 May 2017 24 June 2017	17 January 2017 13 February 2017 29 March 17 14 July 2017 14 August 2017 19 September 2017

LANDSAT 8 and ASTER images were atmospherically and topographically corrected using the Atmospheric/Topographic Correction for Mountainous Terrain (ATCOR) software developed by the German Aerospace Center, Wessling, Germany [33]. MODIS and SENTINEL 3 data do not require such corrections. All images in Table 1 are geometrically matched to each other.

2.4. Calculation of ETo Using Meteorological Data

There are five Davis Vantage Pro weather stations in the study area. These stations are part of a network owned by Universidad Técnica Particular de Loja (Table 2), which collects information on maximum, minimum and average air temperatures (T_a); relative humidity (HR); wind speed (U_2); and shortwave solar radiation (R_s) with a temporal resolution of 10 min.

Table 2. Weather stations in the study area.

Station	Longitude	Latitude	Elevation (masl)
Militar	79°13′03.1″W	03°56′52.6″S	2033
Jipiro	79°11′23.5″W	03°58′15.7″S	2218
Tecnico	79°14′59.6″W	03°59′14.9″S	2377
Ventanas	79°14′46.0″W	04°01′18.9″S	2816
Villonaco	79°16′09.9″W	03°59′10.6″S	2952

Equation (1) was applied to calculate the daily reference crop evapotranspiration using the recorded variables. Further details on the calculation of ETo can be found in [4,34].

2.5. Calculation of ETo Using Remote Sensing Data

For LANDSAT 8 and ASTER, the surface temperature (T_s) was calculated by applying the following equation [35]:

$$T_s = \frac{T_b}{1 + \left(\frac{\lambda * T_b}{\alpha}\right) * ln(\varepsilon)} \tag{2}$$

where T_s is the surface temperature (K), T_b is the brightness temperature (K), λ is the effective wavelength of the thermal band (µm), $\alpha = \text{h c}/\sigma\left(1.438 \times 10^{-2}\ \text{mK}\right)$, h is Planck's constant (6.626×10^{-34} J s^{-1}), c is the speed of light (2.998×10^{8} m s^{-1}), σ is the Stefan Boltzmann constant (1.38×10^{-23} J K^{-1}) and ε is the surface emissivity.

The emissivity was estimated using the following equation [36]:

$$\varepsilon = \varepsilon_{\text{V}}\text{PV} + \varepsilon_{\text{SU}}(1 - \text{PV}) \tag{3}$$

where ε is the emissivity of the surface, ε_{V} is the emissivity of the vegetation (0.985), ε_{SU} is the emissivity of the soil (0.960) and PV is the vegetation proportion, which can be determined by the following equation [37]:

$$PV = \left(\frac{NDVI - NDVI_{min}}{NDVI_{max} - NDVI_{min}}\right)^2 \tag{4}$$

where $NDVI_{max}$ and $NDVI_{min}$ are the maximum and minimum values of the normalized difference vegetation index.

Band 9 of the images obtained by the SLSTR sensor was used for SENTINEL 3. In the case of MODIS, the temperature maps were obtained from the MOD11A1 product.

The air temperature (T_a) was calculated using multiple regression equations, applying the methodology proposed by [38]. The independent variables considered were the soil temperature (T_s) (calculated with Equation (2)) and the elevation (z) extracted from a 30 m resolution DEM that was downloaded from the Alaska Satellite Facility Distributed Active Archive Center (ASF DAAC). The Ta values registered in the existing meteorological stations in the study area (Table 2) were considered as dependent variables.

The instantaneous net radiation was calculated by applying the following equation [39]:

$$R_{ni} = 0.77Rs_{\downarrow} + 0.98\left(Rl_{\downarrow} - \sigma Ts^4\right) \tag{5}$$

where R_{ni} is the instantaneous net surface radiation (w m^{-2}), $Rs_{\downarrow}$ is the incoming shortwave solar radiation (w m^{-2}), Ts is the surface temperature (K) and σ is the Stefan Boltzmann constant (5.67 $\times$ 10^{-8} W m^{-2} K^{-4}).

To determine the daily net radiation R_{nd}, the equation from [7] was used:

$$R_{nd} = C_d R_{ni} \tag{6}$$

$$C_d = \frac{(1-\alpha)Rs_{\downarrow d} + \varepsilon\left(Rl_{\downarrow d} - \sigma {T_{sd}}^4\right)}{(1-\alpha)Rs_{\downarrow i} + \varepsilon\left(Rl_{\downarrow i} - \sigma {T_{si}}^4\right)} \tag{7}$$

where $Rs_{\downarrow d}$ is the daily incoming shortwave solar radiation (W m^{-2}), $Rs_{\downarrow i}$ is the instantaneous incoming shortwave solar radiation (W m^{-2}), $Rl_{\downarrow d}$ is the daily instantaneous downward longwave radiation (w m^{-2}), $Rl_{\downarrow i}$ is the instantaneous downward longwave radiation (w m^{-2}), T_{sd} is the daily surface temperature (K), T_{si} is the instantaneous surface temperature (K), α is the albedo and ε is the emissivity.

Albedo (α) was determined using the following equation [7]:

$$\alpha = \frac{1}{2}(\rho_{RED} + \rho_{NIR}) \tag{8}$$

where ρ_{RED} and ρ_{NIR} are, respectively, the RED and NIR reflectances.

$Rs_{\downarrow d}$ and $Rs_{\downarrow i}$ were calculated using information recorded at weather stations. The descending longwave radiation $Rl_{\downarrow d}$ was estimated using the following equation [2,40]:

$$Rl_{\downarrow d} = 1.24\left(\frac{e_a}{T_a}\right)^{\frac{1}{7}} \sigma {T_a}^4 \tag{9}$$

$$e_a = 6.108\, e^{\left(17.27 \frac{(T_a - 273.15)}{(T_a - 35.85)}\right)} \left(\frac{HR}{100}\right) \tag{10}$$

where e_a is the actual vapor pressure (HPa), and T_a is the air temperature (K).

The soil heat flux was calculated using the following equation [41]:

$$G = \left(\left(0.0038\alpha + 0.0074\alpha^2\right)\left(1 - 0.98NDVI^4\right)\frac{(Ts - 273.15)}{\alpha}\right)Rnd \tag{11}$$

Equation (1) was applied to calculate the regional ETo using the results obtained from the remote sensing products described in this section; wind speed, radiation and relative humidity data, recorded at the meteorological stations, were spatialized using the ordinary Kriging interpolation method [29,41] through the use of geographic information systems (GISs). Kriging is a method that originates in geological and mining applications that assumes there is a non-random relationship between the points that changes spatially. The geostatistical interpolation consists in making an optimal prediction of field values in a place where no data is available by using known data to elaborate a field variogram (covariance), thus providing a prediction and its error considering certain weighting factors [42]

The data to be interpolated were adjusted satisfactorily to a normal distribution, observing the existence of a second-order trend. With these considerations, it was decided to perform an ordinary Kriging interpolation without any transformation, with second-order trend removal and adjustment of a spherical semivariogram, which, according to [43], should have been adequate due to the nature of the data.

2.6. Product Evaluation

The results obtained using the data from LANDSAT 8, SENTINEL 3, ASTER and MODIS were evaluated through cross-validation. The ETo was calculated at a regional scale for each selected date, leaving one station at a time out of the calculations. The point value corresponding to the spatial location of the station not considered was extracted to relate it to the one calculated in the traditional way. The coefficient of determination

(R^2), the Nash–Sutcliffe efficiency (NSE) and the root mean square error (RMSE) [41] were calculated to quantitatively assess the accuracy of the ETo estimates.

3. Results and Discussion

An inverse relationship exists between the elevation above sea level (z) and the air temperature, as can be observed in the regression equations for each date considered (Table 3). On the other hand, a more variable relationship between air temperature and ground temperature (T_s) can also be observed, which was produced by the particular conditions of the moment of observation.

Table 3. Multiple regression equations to calculate T_a.

Date	Sensor	Equation to Calculate T_a (°C)
7 January 2017	LANDSAT 8	$T_a = 31.901 - 0.00786z + 0.0893T_s$
17 January 2017	MODIS	$T_a = 79.961 - 0.01546z - 1.1131T_s$
13 February 2017	MODIS	$T_a = 27.239 - 0.00675z + 0.1313T_s$
29 March 2017	MODIS	$T_a = 38.777 - 0.008317z - 0.133T_s$
7 May 2017	ASTER	$T_a = 28.963 - 0.00585z + 0.01104T_s$
	SENTINEL 3	$T_a = 34.6518 - 0.00733z - 0.1604T_s$
24 June 2017	ASTER	$T_a = 28.991 - 0.00663z + 0.05198T_s$
	SENTINEL 3	$T_a = 21.7586 - 0.00625z + 0.3755T_s$
14 July 2017	SENTINEL 3	$T_a = 31.7595 - 0.00771z + 0.0356T_s$
	MODIS	$T_a = 30.696 - 0.00723z + 0.0220T_s$
14 August 2017	MODIS	$T_a = 40.953 - 0.00875z - 0.2319T_s$
19 August 2017	LANDSAT 8	$T_a = 25.822 - 0.00414z - 0.0000201T_s$
19 September 2017	MODIS	$T_a = 8.785 - 0.004197z - 0.5991T_s$
20 September 2017	LANDSAT 8	$T_a = 34.122 - 0.00837z + 0.0667T_s$
	SENTINEL 3	$T_a = 31.288 - 0.00783z + 0.1384T_s$

High variability was observed in the ETo values (Table 4), which was attributed to the influence of local conditions caused by the presence of marked altitude differences that lead to differences in temperature, wind speed, incident radiation, etc., causing low uniformity in the ETo values.

Table 4. ETo values for the selected dates at the existing stations in the study area.

Date	Militar	Jipiro	Tecnico	Ventanas	Villonaco
7 January 2017	2.80	1.52	2.00	0.90	5.94
17 January 2017	3.54	3.77	4.23	0.40	3.15
13 February 2017	3.86	3.72	3.08	4.07	3.55
29 March 2017	2.46	3.00	2.94	1.98	3.05
7 May 2017	1.91	2.28	2.93	1.74	4.56
24 June 2017	2.74	3.23	2.44	2.97	5.15
14 July 2017	2.06	3.21	3.31	3.20	4.86
14 August 2017	3.45	3.63	3.49	3.36	4.85
19 August 2017	2.61	2.90	3.07	3.31	3.07
19 September 2017	3.73	4.00	3.79	2.80	2.75
20 September 2017	3.84	4.70	4.09	3.59	3.43

Additionally, no seasonal behavior was observed in the study area. This was because it is located on the equator, in an inter-Andean valley influenced by the climatic regime of the Pacific Ocean (wet season from December to April) and the climatic regime of the Amazonia (humid almost all year round), with average temperature fluctuations of no more than 2 °C. This produces uniform climatic conditions to some extent throughout the year [30].

Some examples of the surface temperature calculated using the products obtained by remote sensing are shown in Figure 2. The influence of the spatial resolution of the images can be observed, with the LANDSAT results being the most detailed. On the other hand, the spatial distribution of the temperature shows that the highest values of Ts were at the lowest elevations (in the valley of the study area) where the city of Loja is located. The surrounding areas of the city are covered by vegetation and present a higher albedo than the valley, consequently registering a lower surface temperature. The valley is surrounded by mountains, so the lowest Ts values are recorded in the periphery of the study area.

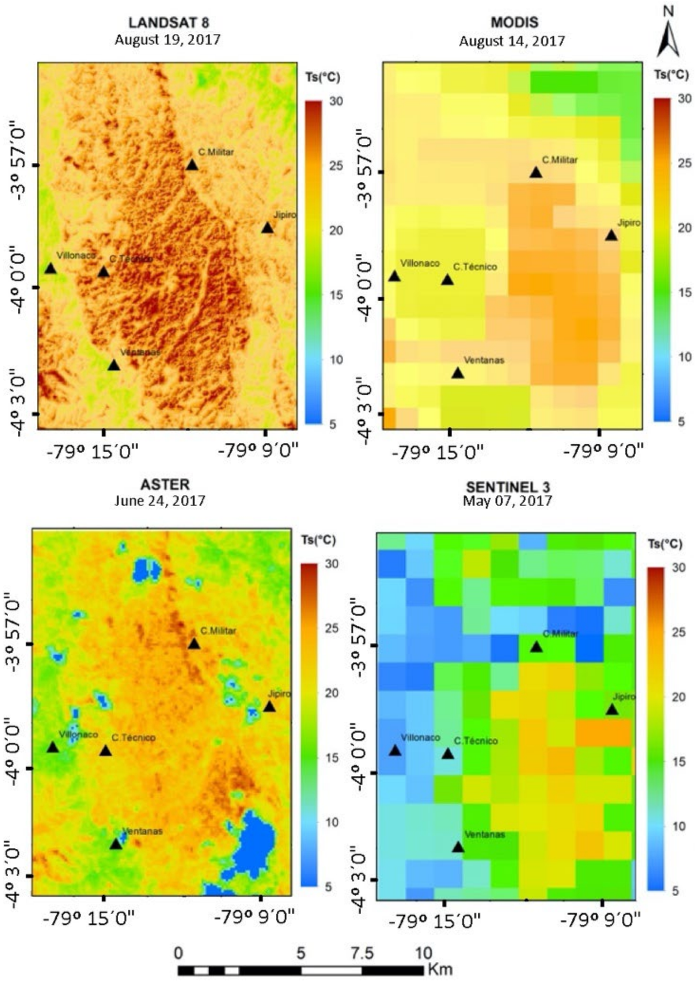

Figure 2. Surface temperature (°C) for the different satellite products.

Similar behavior was observed in the air temperature maps presented in Figure 3, where the distribution of Ta is more uniform. Additionally, the inverse proportionality between the elevation and Ta can be observed.

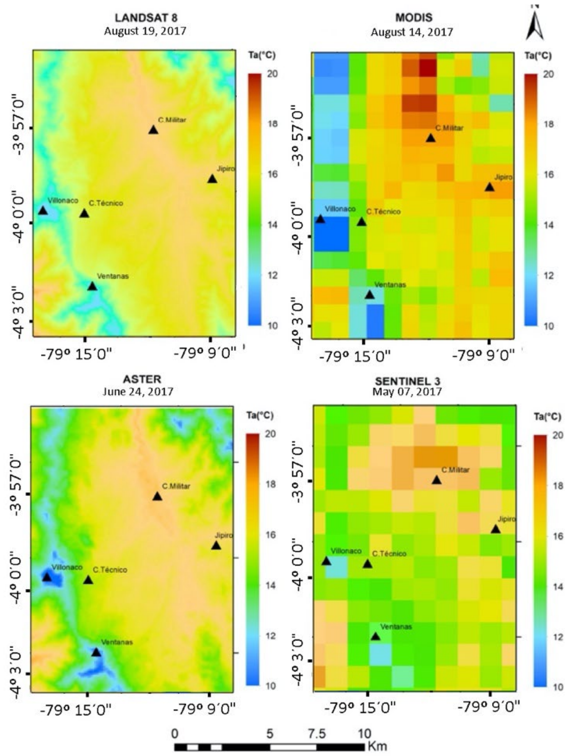

Figure 3. Air temperature (°C) for the different satellite products.

The spatial variation of the net radiation is presented in Figure 4. The highest values are located in the areas with the highest elevation, which are covered by forests in good condition. The spatial variability of the ETo is high (Figure 5) due to the variable conditions of temperature, net radiation, wind speed, etc.

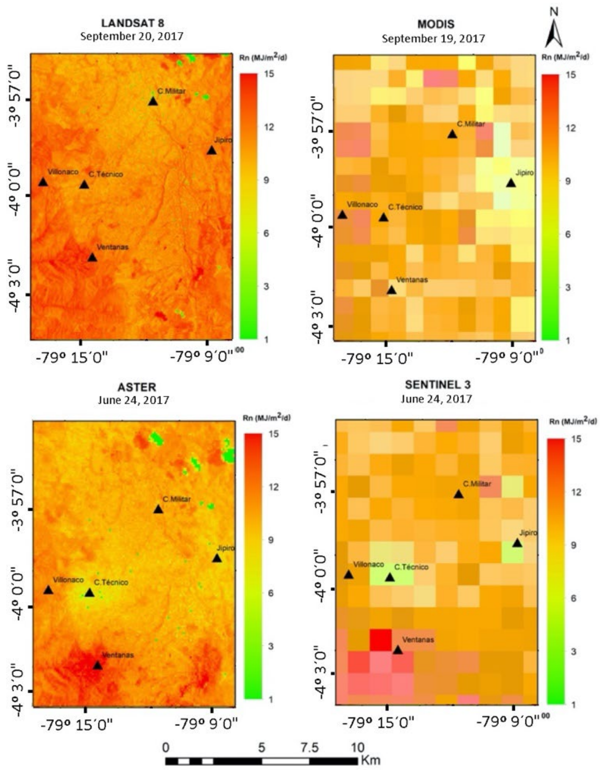

Figure 4. Daily net radiation (Rn) (MJ m^{-2} day^{-1}) for the different products.

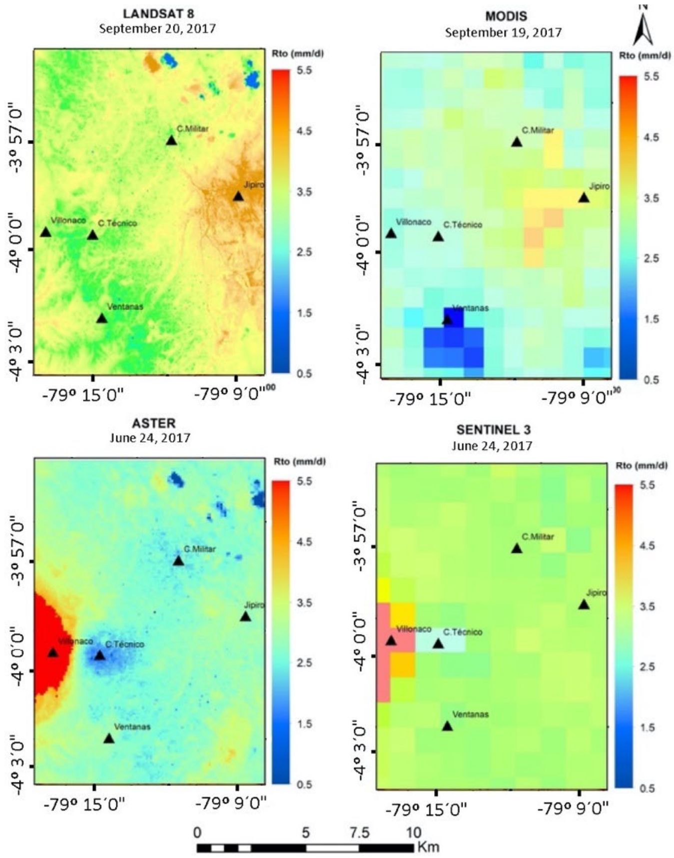

Figure 5. Maps of ETo (mm day^{-1}) for the different satellite products.

The ETo values for the selected dates at the existing stations in the study area calculated using remote sensing data (Table 5) are similar to those presented in Table 4. On the dates in which information from two sensors is available, it is possible to see values that have a certain similarity, with the exception of 5 July 2017, in which the values calculated using ASTER and MODIS data present much greater differences. This may have originated in the spatial resolution of the sensors, since MODIS presents larger pixels in contrast to ASTER, which has a better level of detail thanks to its better spatial resolution.

Table 5. ETo values for the selected dates at the existing stations in the study area calculated using remote sensing data.

Date	Sensor	Militar	Jipiro	Tecnico	Ventanas	Villonaco
7 January 2017	LANDSAT	2.56	1.67	2.20	1.00	5.99
17 January 2017	MODIS	2.78	3.11	3.06	0.37	2.70
13 February 2017	MODIS	3.45	3.37	2.47	3.37	2.96
29 March 2017	MODIS	2.25	2.88	2.44	1.75	3.05
7 May 2017	ASTER	2.01	2.02	2.04	1.56	4.53
	SENTINEL 3	1.99	1.50	2.54	1.35	4.21
24 June 2017	ASTER	2.65	3.15	2.00	3.09	5.19
	SENTINEL 3	2.87	2.95	2.28	2.73	4.68
14 July 2017	SENTINEL 3	2.85	3.12	3.11	3.09	4.56
	MODIS	2.27	3.35	2.96	3.01	4.86
14 August 2017	MODIS	3.37	3.65	3.01	3.03	4.80
19 August 2017	LANDSAT	2.33	2.80	2.63	3.32	3.08
19 September 2017	MODIS	3.24	3.53	2.95	2.26	2.75
20 September 2017	LANDSAT	3.46	4.61	3.52	3.49	3.57
	SENTINEL 3	3.65	4.23	3.50	3.10	3.43

The absolute values of the differences between the ETo calculated with station data and the ETo calculated with remote sensing data are presented in Table 6. On the days in which MODIS data were used, a greater absolute values for the differences were observed, reaching a maximum mean value of 0.61 mm with a standard deviation of 0.42 mm (01/17/17). Differences were observed for the dates in which LANDSAT 8 and ASTER data were used with values of 0.15 mm and deviations of 0.08 mm and 0.16 mm.

Table 6. Absolute values of differences between ETo calculated with station data and ETo calculated with remote sensing data.

Date	Sensor	Militar	Jipiro	Tecnico	Ventanas	Villonaco	AVG	STD
7 January 2017	LANDSAT 8	0.24	0.15	0.20	0.10	0.05	0.15	0.08
17 January 2017	MODIS	0.76	0.66	1.17	0.03	0.45	0.61	0.42
13 February 2017	MODIS	0.41	0.35	0.61	0.70	0.59	0.53	0.15
29 March 2017	MODIS	0.21	0.12	0.50	0.23	0.00	0.21	0.18
7 May 2017	ASTER	0.10	0.26	0.89	0.18	0.03	0.29	0.35
	SENTINEL 3	0.08	0.78	0.39	0.39	0.35	0.40	0.25
24 June 2017	ASTER	0.09	0.08	0.44	0.12	0.04	0.15	0.16
	SENTINEL 3	0.13	0.28	0.16	0.24	0.47	0.26	0.13
14 July 2017	SENTINEL 3	0.79	0.09	0.20	0.11	0.30	0.30	0.29
	MODIS	0.21	0.14	0.35	0.19	0.00	0.18	0.13
14 August 2017	MODIS	0.08	0.02	0.48	0.33	0.05	0.19	0.20
19 August 2017	LANDSAT 8	0.28	0.10	0.44	0.01	0.01	0.17	0.19
19 September 2017	MODIS	0.49	0.47	0.84	0.54	-	0.59	0.17
20 September 2017	LANDSAT 8	0.38	0.09	0.57	0.10	-	0.29	0.23
	SENTINEL 3	0.19	0.47	0.59	0.49	-	0.44	0.17
AVG		0.30	0.27	0.52	0.25	0.20		
STD		0.23	0.05	0.08	0.04	0.05		

The smallest values of the average and standard deviation, were observed in the Villonaco station (Table 7), in which, again, LANDSAT 8 and ASTER showed lower average values—0.02 mm and 0.03 mm, respectively—while the average values obtained by Sentinel 3 and MODIS were significantly higher (0.28 mm and 0.18 mm, respectively). The resolution of each sensor could cause the difference between these values.

Table 7. Average and standard deviation of the absolute values of the differences between ETo calculated with station data and ETo calculated with remotely sensed data (Table 6), by sensor and station.

Sensor	Parameter	Militar	Jipiro	Tecnico	Ventanas	Villonaco
LANDSAT 8	Average	0.30	0.11	0.40	0.07	0.02
	STD	0.07	0.03	0.19	0.05	0.03
ASTER	Average	0.10	0.17	0.67	0.15	0.03
	STD	0.01	0.13	0.32	0.04	0.01
SENTINEL 3	Average	0.30	0.41	0.34	0.31	0.28
	STD	0.33	0.29	0.20	0.17	0.09
MODIS	Average	0.36	0.29	0.66	0.34	0.18
	STD	0.25	0.24	0.30	0.25	0.28

The comparison between the remote sensing data ETo and the station data ETo (Figure 6) presented a good fit, especially when data from LANDSAT 8 and ASTER were used. On the other hand, a large dispersion was observed for the results obtained with MODIS; the detail level of the satellite images and products is decisive.

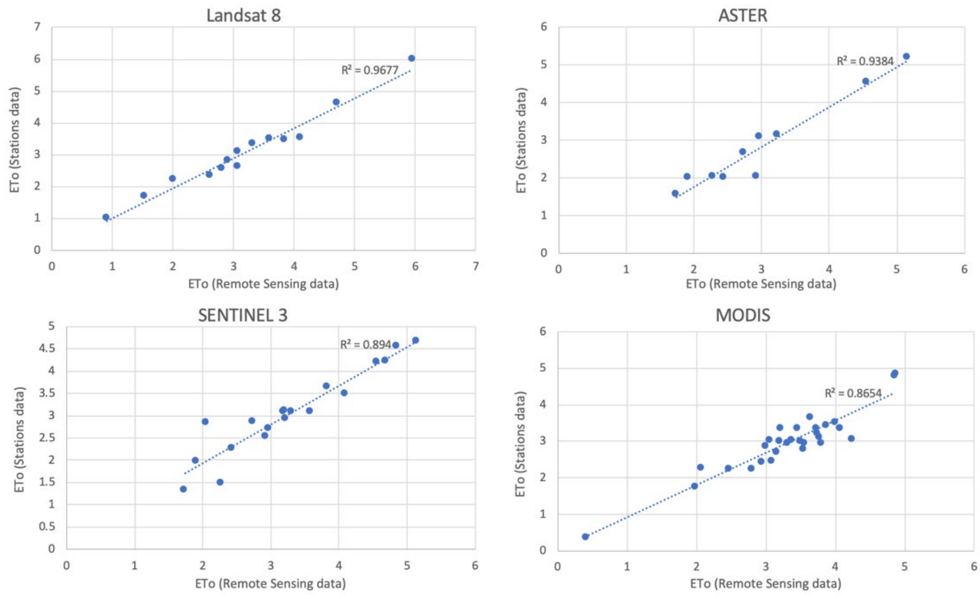

Figure 6. Comparison between remote sensing data ETo and the station data ETo.

All validation parameters for the ETo estimates (R^2, NSE and RMSE) obtained from satellite products were in very satisfactory ranges (Table 8). ASTER and LANDSAT 8 products presented the best results, which can be attributed to their good spatial resolution. This also occurred with the other products, the precision of which decreased as their spatial resolution decreased. The effect of resolution was notable since the radiometric response for the same portion of the territory differs depending on the size of the pixel. This is because, with larger pixels, greater numbers of land covers will be considered to average the information, which causes a decrease in the precision of the ETo estimates.

Table 8. Validation parameters.

Sensor	NSE	R^2	RMSE
LANDSAT 8	0.994	0.968	0.060
ASTER	0.988	0.938	0.067
SENTINEL 3	0.985	0.894	0.110
MODIS	0.979	0.865	0.160

In contrast to this, the temporal resolutions of SENTINEL 3 and MODIS are significantly higher than those of LANDSAT 8 and ASTER (see Table 1). This implies the availability of a greater number of images. Although the accuracy obtained by SENTINEL 3 and MODIS was lower than that obtained by LANDSAT 8 and ASTER (see Table 8), their resolution is acceptable and, therefore, they constitute an important alternative in cases where permanent monitoring of the ETo is required or in areas characterized by frequent cloud cover.

4. Conclusions

The results show that the precision of the calculations is proportional to the spatial resolution. Higher spatial resolutions reach close-to-optimum values for the coefficient of determination (R^2), Nash–Sutcliffe efficiency (NSE) and root mean square error (RMSE). This translates into very satisfactory ETo estimates when using LANDSAT 8 and ASTER products.

The temporal resolutions of MODIS and SENTINEL 3 products is significantly higher than those of the LANDSAT 8 and ASTER products. Therefore, although the precision of ETo estimations using MODIS and SENTINEL 3 is lower than that obtained with LANDSAT 8 and MODIS, they can be used in applications that require continuous monitoring of ETo.

Finally, LANDSAT 8 sensor products result in greater precision in ETo estimations, while SENTINEL 3 products constitute the best alternative if continuous monitoring of ETo is preferred over precision.

Although several of the parameters required by the Penman–Monteith equation can be estimated through remote sensing, data measured at meteorological stations are still required to estimate ETo accurately. This could limit the application of the proposed methodology in places where meteorological networks have little coverage. Future works could focus on the estimation of these parameters based on remote sensing in order to reduce dependence on data measured in the field. Furthermore, exploring the applicability of different methodologies for calculating ETo through remote sensing could be relevant. Finally, the study of the relationship between the regional ETo, the climatic variations and the multi-temporal change of land use/cover could potentially contribute to understandings of the implications of climate change in a given territory, assisting in the definition of possible scenarios and outlining adaptation actions.

Author Contributions: Conceptualization, F.O.-V. and A.O.-P.; methodology, F.O.-V. and A.O.-P.; validation, A.O.-P., D.N. and F.O.-V.; formal analysis, F.O.-V.; investigation, A.O.-P.; resources, D.N.; writing—original draft preparation, F.O.-V., A.O.-P. and D.N.; writing—review and editing, F.O.-V.; visualization, D.N.; project administration, F.O.-V.; All authors have read and agreed to the published version of the manuscript.

Funding: This research received no external funding.

Data Availability Statement: Not applicable.

Conflicts of Interest: The authors declare no conflict of interest.

References

1. Walker, E.; García, G.A.; Venturini, V. Estimación de la evapotranspiración real en zonas de llanura mediante productos de humedad de suelo de la misión SMAP. *Rev. Teledetección* **2018**, *52*, 17–26. [CrossRef]
2. Sur, C.; Kang, S.; Kim, J.; Choi, M. Remote sensing-based evapotranspiration algorithm: A case study of all sky conditions on a regional scale. *GISci. Remote Sens.* **2015**, *52*, 627–642. [CrossRef]
3. Marini, F.; Santamaría, M.; Oricchio, P.; Di Bella, C.M.; Basualdo, A. Estimación de evapotranspiración real (ETR) y de evapotranspiración potencial (ETP) en el sudoeste bonaerense (Argentina) a partir de imágenes MODIS. *Rev. Teledetección* **2017**, *48*, 29–41. [CrossRef]
4. Allen, R.; Pereira, L.; Raes, D.; Smith, M. *Crop. Evapotranspiration: Guidelines for Computing Crop Water Requeriments*; FAO Irrigation and Drainage Paper No. 56; Food and Agriculture Organization of the United Nations: Rome, Italy, 1998; p. 338.
5. Sánchez, M.; Chuvieco, E. Estimación de la evapotranspiración del cultivo de referencia, ET0, a partir de imágenes NOAA-AVHRR. *Rev. Teledetección* **2000**, *14*, 11–21.
6. Rivas, R.; Caselles, V. A simplified equation to estimate spatial reference evaporation from remote sensing-based surface temperature and local meteorological data. *Remote Sens. Environ.* **2004**, *93*, 68–76. [CrossRef]
7. Sobrino, J.A.; Gómez, M.; Jiménez-Muñoz, J.C.; Olioso, A. Application of a simple algorithm to estimate daily evapotranspiration from NOAA–AVHRR images for the Iberian Peninsula. *Remote Sens. Environ.* **2007**, *110*, 139–148. [CrossRef]
8. Tasumi, M.; Trezza, R.; Allen, R.G.; Wright, J.L. Satellite-Based Energy Balance for Mapping Evapotranspiration with Internalized Calibration (METRIC)-Applications. *J. Irrig. Drain. Eng.* **2008**, *133*, 395–406.
9. Venturini, V.; Islam, S.; Rodríguez, L. Estimation of evaporative fraction and evapotranspiration from MODIS products using a complementary based model. *Remote Sens. Environ.* **2008**, *112*, 132–141. [CrossRef]
10. Barraza, V.; Restrepo-Coupe, N.; Huete, A.; Grings, F.; Van Gorsel, E. Passive microwave and optical index approaches for estimating surface conductance and evapotranspiration in forest ecosystems. *Agric. For. Meteorol.* **2015**, *213*, 126–137. [CrossRef]
11. Knipper, K.; Hogue, T.; Scott, R.; Franz, K. Evapotranspiration estimates derived using multi-platform remote sensing in a semiarid region. *Remote Sens.* **2017**, *9*, 184. [CrossRef]
12. Anderson, M.C.; Norman, J.M.; Diak, G.R.; Kustas, W.P.; Mecikalski, J.R. A two-source time-integrated model for estimating surface fluxes using thermal infrared remote sensing. *Remote Sens. Environ.* **1997**, *60*, 195–216. [CrossRef]
13. Bastiaanssen, W.G.M.; Menenti, M.; Feddes, R.A.; Holtslag, A.A.M. A remote sensing surface energy balance algorithm for land (SEBAL): 1. *Formulation. J. Hydrol.* **1998**, *212*, 198–212. [CrossRef]
14. Allen, R.G.; Tasumi, M.; Trezza, R. Satellite-based energy balance for mapping evapotranspiration with internalized calibration (METRIC)-model. *J. Irrig. Drain. Eng.* **2007**, *133*, 380–394. [CrossRef]
15. Sánchez, J.M.; Scavone, G.; Caselles, V.; Valor, E.; Copertino, V.A.; Telesca, V. Monitoring daily evapotranspiration at a regional scale from Landsat-TM and ETM+data: Application to the Basilicata region. *J. Hydrol.* **2008**, *351*, 58–70. [CrossRef]

16. Jiang, L.; Islam, S. Estimation of surface evaporation map over southern Great Plains using remote sensing data. *Water Resour. Res.* **2001**, *37*, 329–340. [CrossRef]
17. Nishida, K.; Nemani, R.R.; Glassy, J.M.; Running, S.W. Development of an evapotranspiration index from aqua/MODIS for monitoring surface moisture status. *IEEE Trans. Geosci. Remote Sens.* **2003**, *41*, 493–501. [CrossRef]
18. Tang, Q.H.; Peterson, S.; Cuenca, R.H.; Hagimoto, Y.; Lettenmaier, D.P. Satellite-based near- real-time estimation of irrigated crop water consumption. *J. Geophys. Res. Atmos.* **2009**, *114*, D05114. [CrossRef]
19. Castañeda-Ibáñez, C.; Martínez-Menes, M.; Pascual-Ramírez, F.; Flores-Magdaleno, H.; Fernández-Reynoso, D.; Esparza-Govea, S. Estimación de coeficientes de cultivo mediante sensores remotos en el distrito de riego río Yaqui, Sonora, México. *Agrociencia* **2015**, *49*, 221–232.
20. Mu, Q.; Heinsch, F.A.; Zhao, M.; Running, S.W. Development of a global evapotranspiration algorithm based on MODIS and global meteorology data. *Remote Sens. Environ.* **2007**, *111*, 519–536. [CrossRef]
21. Mu, Q.Z.; Zhao, M.S.; Running, S.W. Improvements to a MODIS global terrestrial evapotranspiration algorithm. *Remote Sens. Environ.* **2011**, *115*, 1781–1800. [CrossRef]
22. Zhang, K.; Kimball, J.S.; Mu, Q.; Jones, L.A.; Goetz, S.J.; Running, S.W. Satellite based analysis of northern ET trends and associated changes in the regional water balance from 1983 to 2005. *J. Hydrol.* **2009**, *379*, 92–110. [CrossRef]
23. Fisher, J.B.; Tu, K.P.; Baldocchi, D.D. Global estimates of the land-atmosphere water flux based on monthly AVHRR and ISLSCP-II data, validated at 16 FLUX- NET sites. *Remote Sens. Environ.* **2008**, *112*, 901–919. [CrossRef]
24. Miralles, D.G.; Holmes, T.R.H.; De Jeu, R.A.M.; Gash, J.H.; Meesters, A.G.C.A.; Dolman, A.J. Global land-surface evaporation estimated from satellite- based observations. *Hydrol. Earth Syst. Sci.* **2011**, *15*, 453–469. [CrossRef]
25. Wang, K.C.; Wang, P.; Li, Z.Q.; Cribb, M.; Sparrow, M. A simple method to estimate actual evapotranspiration from a combination of net radiation, vegetation index, and temperature. *J. Geophys. Res. Atmos.* **2007**, *112*, D15107. [CrossRef]
26. Zeng, Z.Z.; Piao, S.L.; Lin, X.; Yin, G.D.; Peng, S.S.; Ciais, P.; Myneni, R.B. Global evapotranspiration over the past three decades: Estimation based on the water balance equation combined with empirical models. *Environ. Res. Lett.* **2012**, *7*, 014026. [CrossRef]
27. Long, D.; Longuevergne, L.; Scanlon, B.R. Uncertainty in evapotranspiration from land surface modeling, remote sensing, and GRACE satellites. *Water Resour. Res.* **2014**, *50*, 1131–1151. [CrossRef]
28. Kumar, U.; Rashmi; Chatterjee, C.; Raghuwanshi, N.S. Comparative Evaluation of Simplified Surface Energy Balance Index-Based Actual ET against Lysimeter Data in a Tropical River Basin. *Sustainability* **2021**, *13*, 13786. [CrossRef]
29. Oñate-Valdivieso, F.; Oñate-Paladines, A.; Collaguazo, M. Spatiotemporal Dynamics of Soil Impermeability and Its Impact on the Hydrology of An Urban Basin. *Land* **2022**, *11*, 250. [CrossRef]
30. Oñate-Valdivieso, F.; Fries, A.; Mendoza, K.; Gonzalez-Jaramillo, V.; Pucha-Cofrep, F.; Rollenbeck, R.; Bendix, J. Temporal and spatial analysis of precipitation patterns in an Andean region of southern Ecuador using LAWR weather radar. *Meteorol. Atmos. Phys.* **2018**, *130*, 473–484. [CrossRef]
31. U.S. Geological Survey (USGS). Earthexplorer. Available online: https://earthexplorer.usgs.gov (accessed on 18 November 2021).
32. Copernicus Open Access Hub. Available online: https://scihub.copernicus.eu/dhus/#/home (accessed on 5 December 2021).
33. Richter, R.; Schläpfer, D. *Atmospheric/Topographic Correction for Satellite Imagery: ATCOR-2/3 User Guide, DLR-IB 565-01/15*; German Aerospace Center: Wessling, Germany, 2015.
34. Jensen, M.E.; Burmann, R.D.; Allen, R.G. Evaporation and Irrigation Water Requirements. In *ASCE Manual and Reports on Engineering Practice*; American Society of Civil Engineers: New York, NY, USA, 2016; Volume 70, p. 360.
35. Li, Y.Y.; Liu, Y.; Ranagalage, M.; Zhang, H.; Zhou, R. Examining land use/land cover change and the summertime surface urban heat island effect in fast-growing greater hefei, China: Implications for sustainable land development. *ISPRS Int. J. Geo-Inf.* **2020**, *9*, 568. [CrossRef]
36. Valor, E.; Caselles, V. Mapping land surface emissivity from NDVI: Application to European, African, and South American areas. *Remote Sens. Environ.* **1996**, *57*, 167–184. [CrossRef]
37. Meng, X.; Cheng, J.; Zhao, S.; Liu, S.; Yao, Y. Estimating Land Surface Temperature from Landsat-8 Data using the NOAA JPSS Enterprise Algorithm. *Remote Sens.* **2019**, *11*, 155. [CrossRef]
38. Ninyerola, M.; Pons, X.; Roure, J.M. A methodological approach of climatological modelling of air temperature and precipitation. *Int. J. Climatol.* **2000**, *20*, 1823–1841. [CrossRef]
39. Carmona, F.; Rivas, R.; Kruse, E. Estimating daily net radiation in the FAO Penman-Monteith method. *Theor. Appl. Climatol.* **2017**, *129*, 89–95. [CrossRef]
40. Bastiaanssen, W.G. SEBAL-based sensible and latent heat fluxes in the irrigated Gediz Basin, Turkey. *J. Hydrol.* **2000**, *229*, 87–100. [CrossRef]
41. Oñate-Valdivieso, F.; Uchuari, V.; Oñate-Paladines, A. Large-Scale Climate Variability Patterns and Drought: A Case of Study in South—America. *Water Resour. Manag.* **2020**, *34*, 2061–2079. [CrossRef]
42. Karavitis, C.A.; Alexandris, S.G.; Tsesmelis, D.E.; Athanasopoulos, G. Application of the Standardized Precipitation Index (SPI) in Greece. *Water* **2011**, *3*, 787–805. [CrossRef]
43. Goovaerts, P. Geostatistical approaches for incorporating elevation into the spatial interpolation of rainfall. *J. Hydrol.* **2000**, *228*, 113–129. [CrossRef]